Mechanochemical Synthesis

CrossMark

F anion dynamics in cation-mixed nanocrystalline LaF$_3$: SrF$_2$

S. Breuer[1], S. Lunghammer[1], A. Kiesl[1], and M. Wilkening[1,*] (ORCID)

[1] *Christian Doppler Laboratory for Lithium Batteries, and Institute for Chemistry and Technology of Materials, Graz University of Technology (NAWI Graz), Stremayrgasse 9, 8010 Graz, Austria*

ABSTRACT

Ion dynamics in nanocrystalline materials can be quite different compared to that in materials with μm-sized crystallites. In particular, the substitution of iso- or aliovalent ions opens pathways to systematically control ion transport properties. Here we studied the incorporation of SrF$_2$ into the tysonite structure of LaF$_3$ and its effect on F$^-$ transport. High-energy ball milling directly transforms the binary fluorides in a structurally disordered, phase pure nanocrystalline ceramic. Compared to Sr-free LaF$_3$, ionic conductivity could be increased by several orders of magnitude. We attribute this enhancement to the generation of lattice strain and the formation of F defect sites. In agreement with this increase, the activation energy E_a of long-range ionic transport in the solid solution La$_{1-x}$Sr$_x$F$_{3-x}$ significantly decreases from 0.75 eV ($x = 0$) to 0.49 eV ($x = 0.1$).

Introduction

Ionic conductors take on an essential rôle in materials science [1, 2]. They constitute an important part in many devices such as sensors [3] and those constructed for electrochemical energy storage [4, 5]. Apart from Li and Na ion conductors, also materials with high F anion conductivity have increasingly attracted attention [6], because there is renewed interest in the realization of batteries with fluorine anions as main charge carriers [7–9]. Apart from that, binary earth alkaline fluorides, especially CaF$_2$ and BaF$_2$, easily accept rare-earth-elements and, thus, allow the preparation of luminescent solid solutions with improved optical properties. Considering lanthanum, the ionic radius of La^{3+} (103 pm) is very similar to that of Ca^{2+} in CaF$_2$ (100 pm); it is, however, somewhat smaller than the cation radius of Sr^{2+} (118 pm) in cubic SrF$_2$ (Fig. 1). Recently, La$_{1-x}$Ba$_x$F$_{3-x}$ solid solutions with $x = 0.1$ have been introduced as promising ion conductor for F-ion battery systems [8, 10]. Ba^{2+} has a larger ionic radius (135 pm) than La^{3+}. Starting with undoped LaF$_3$ it is expected that also the ionic conductivity of nanocrystalline La$_{1-x}$Sr$_x$F$_{3-x}$ (with $x \leq 0.1$) significantly changes with SrF$_2$ incorporation [11]. As seen for other systems, see Ref. [12] for a brief review on fluorides, we expect lattice strain and distortions [13–15], caused by the difference in ionic radii, to promote ionic transport.

Address correspondence to E-mail: wilkening@tugraz.at

Springer
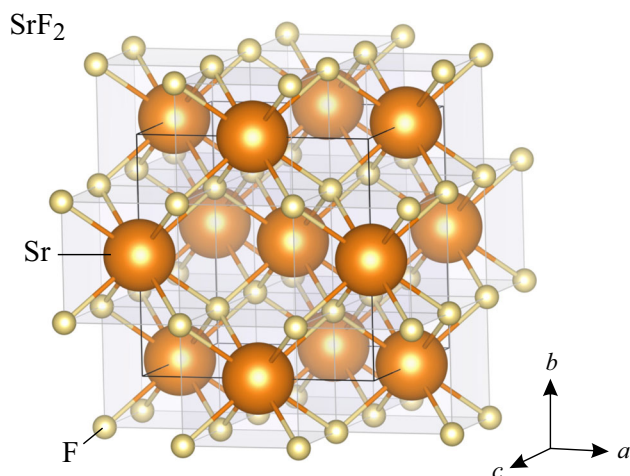
Figure 1 Crystal structure of SrF_2. Strontium fluoride crystallizes with cubic symmetry ($Fd\bar{3}m$); F anions occupy the same crystallographic position ($8c$) which produces a single resonance in ^{19}F NMR spectroscopy.

Here, we used high-energy ball milling to prepare a series of nanocrystalline $La_{1-x}Sr_xF_{3-x}$ samples and studied (local) structures as well as long-range F anion transport. While Sr^{2+} crystallizes with cubic symmetry (Fig. 1), LaF_3 adopts the more complex tysonite structure, see Fig. 2. During ball milling the number density of defect sites usually increases which causes the bulk ionic conductivity also to increase as compared to the more ordered, single crystalline state. This effect has, in particular, been shown for oxides such as $LiNbO_3$ [16] and $LiTaO_3$ [17]. Recently, a quite similar enhancement has been reported for $LiAlO_2$ [18] and Li_2TiO_3 [19]. We expect that a measurable increase is also seen for ball milled SrF_2 and LaF_3. Whereas in SrF_2 only one crystallographic F site exist, in LaF_3 three crystallographically distinct F sites can be found [20]. The F1 anions residing on $12g$ are located in the $_\infty[F_{2-x}]^{-2+x}$ interslab. F3 and F2 anions are found in or near the La layers, see Fig. 2. In the pioneering work of Wang and Grey F anion exchange processes in LaF_3 were studied by high-resolution solid-state nuclear magnetic resonance (NMR) spectroscopy. It turned out that fast F1-F1 exchange processes markedly determine ionic conductivity in the tysonite structure, whereas the F1-(F2,F3) hopping processes are less frequent.

In general, ball milling is a versatile method not only to prepare single-phase nanostructured materials but also to induce and to carry out mechanochemical reactions [12, 21]. The latter often lead to non-equilibrium (or metastable) compounds that cannot be prepared via conventional high-temperature synthesis routes [12]. Apart from that, high-energy ball milling is also useful to prepare phases, which are only stable at high pressures. As an example, mechanical treatment of γ-$LiAlO_2$ leads to the formation of several modifications which are usually observed at high pressures [18]. If cubic BaF_2 is ball milled for several hours in planetary mills one can follow the generation of orthorhombic BaF_2 by both X-ray diffraction and high-resolution ^{19}F nuclear magnetic resonance (NMR) [14]. In the present case we used mechanical treatment to force the cations to mix on atomic scale. The major component, which is, if not stated otherwise, LaF_3, determines the final crystal structure, i.e., the smaller Sr^{2+} ions are incorporated into the tysonite structure. In many cases phase pure mixed compounds are available by ball milling under dry conditions [22, 23]. The effect of abraded material from vial sets and milling balls has only a negligible effect if other factors, such as cation mixing, governs ion dynamics [14]. As has been documented for other nanocrystalline systems, the main change in ionic conductivity is caused by structural disorder, lattice strain introduced and the mixed cation effect [15–17]. The mismatch in size of the cations sensitively changes the potential landscape the mobile F anions are exposed to. In our case, because of charge balance, the replacement of La^{3+} by Sr^{2+} also leads to the formation of F vacancies in the anion sublattice. Vacant F sites are anticipated to further boost ion conductivity in nanocrystalline LaF_3, i.e., it is expected to control overall ionic conductivity for samples with $x > 0$. Of course, cation-mixed fluorides can also be prepared via alternative solid-state routes requiring, however, relatively high calcination temperatures. As an example, Chable et al. and Dieudonné et al. studied ion dynamics in $La_{1-x}Ba_xF_{3-x}$ ($x < 0.15$) and $Sm_{1-x}Ca_xF_{3-x}$ ($x < 0.17$) solid solutions, respectively [24–26].

Experimental

Nanocrystalline solid solutions of $La_{1-x}Sr_xF_{3-x}$ with $0.01 \leq x \leq 0.1$ were prepared via high-energy ball milling. We used a planetary mill (Fritsch P7, Premium line) and treated the various mixtures of LaF_3 and SrF_2 in cups made of ZrO_2 (45 mL, Fritsch). Milling was
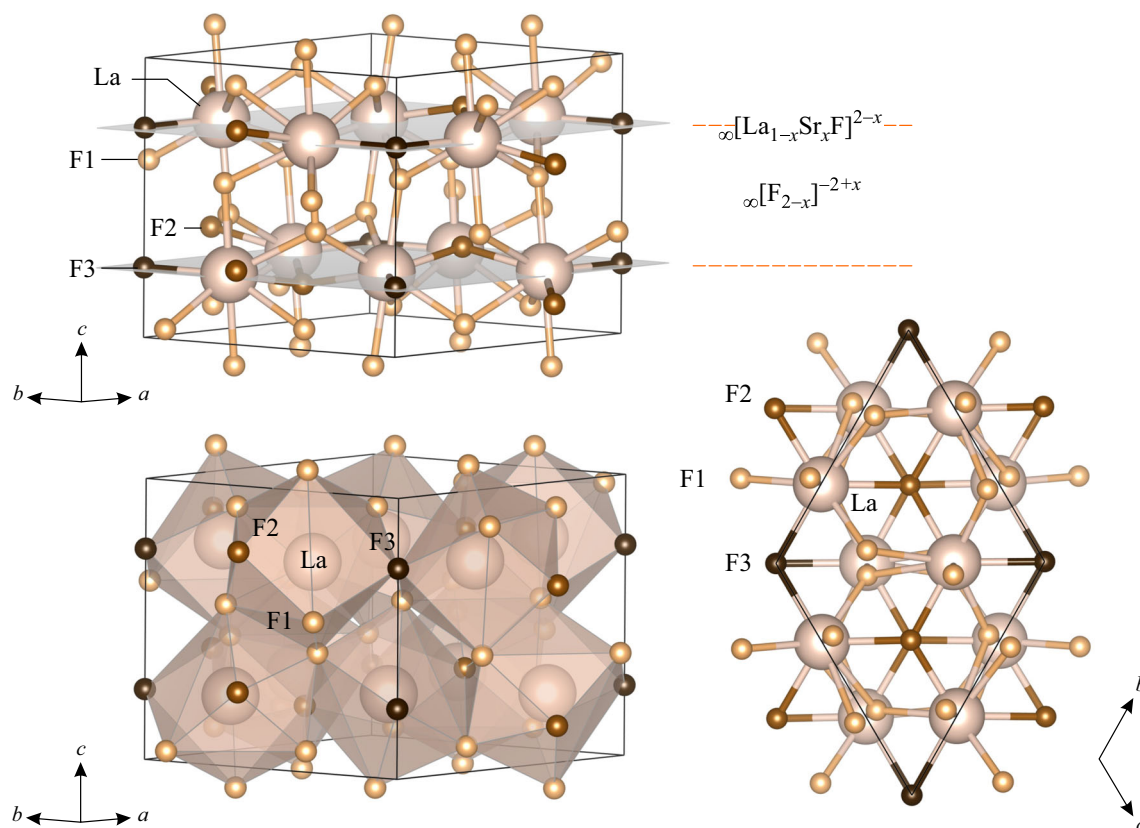
Figure 2 Crystal structure of LaF$_3$ ($P\bar{3}c1$, $Z = 6$). The tysonite structure provides 3 different F sites labeled F1 (12g, C_1 or distorted T_d point symmetry), F2 (4d, C_{3v} point symmetry), and F3 (2a, D_{3h} point symmetry). Each site is fully occupied by fluorine anions. F1 anions reside in the $_\infty[F_{2-x}]^{-2+x}$ interslab. These ions are located in distorted La$_4$ tetrahedra.

carried out with 180 zirconium oxide milling balls (5 mm in diameter). Prior to the milling process, the starting materials were dried at 200°C under vacuum. The subsequent preparation steps were carried out in inert gas atmosphere by taking advantage of Ar-filled gloveboxes (O$_2$, H$_2$O < 0.1 ppm). A milling time of 10 h (600 rpm) leads to almost full incorporation of SrF$_2$ into LaF$_3$. After each 30 min we interrupted the milling process for 15 min to let the vial cool down to room temperature. According to our experience, this way of milling ensures that the temperature of the vial during milling does not exceed values above 60 to 80°C.

The phase purity of the samples prepared was checked by both X-ray diffraction (Bruker D8 Advance, Bragg Brentano geometry, 40 kV) and ^{19}F magic angle spinning (MAS) NMR spectroscopy. Analyzing the reflections of the nanocrystalline materials with the Scherrer equation [27, 28] resulted in mean crystallite sizes in the order of 14 to 20 nm, see also Refs. [17, 22, 23] for similar analyses on

nanocrystalline oxides that partly also considered the effect of lattice strain on samples prepared mechanochemically.

To probe local magnetic environments of the F spins, we recorded rotor-synchronized NMR Hahn echoes by employing a Bruker 1.3-mm MAS probe placed in a 11.4 T cryomagnet (470.39 MHz). This probe allowed us to spin the rotor at frequencies as high as 60 kHz. Spectra were measured with a two pulse (90°-t_p-180°) sequence using a Bruker Avance 500 spectrometer. The 90° pulse length was 1.5 μs at a power level of 50 W. Between each scan a recycle delay of 30 s was ensured to consider almost full longitudinal relaxation. Up to 64 transients were accumulated for a single spectrum, see Figs. 4 and 5. We took advantage of LiF powder as a secondary reference ($- 204.3$ ppm) [29] to determine chemical shifts δ_{iso}; CFCl$_3$ (0 ppm) served as the primary reference.

Ionic conductivities of the pressed powders were analyzed with a Novocontrol Concept 80 broadband spectrometer. To prepare pellets for the impedance measurements the powders were uniaxially cold-pressed at ca. 1 GPa. With the pressing tools available in our laboratory we prepared pellets with a diameter of 8 mm and thicknesses varying from 0.5 to 1 mm. Sputtering was used to apply electrically conducting Au electrodes (100 to 200 nm in thickness). The pellets were placed in a ZGS active cell (Novocontrol). The temperature in the sample chamber was controlled by a QUATRO cryo system (Novocontrol) that allows precise settings of temperature as well as a fully automatic execution of the measurements for a range of temperatures. A stream of freshly evaporated nitrogen gas, which passes a heater before entering the sample chamber, is used to ensure stable stability (± 2 K). For the conductivity (and impedance) measurements we used a voltage amplitude of 100 mV and varied the frequency v from 0.1 Hz to 10 MHz. Specific conductivities were calculated by taking into account the cell constant, i.e., diameter and thicknesses of the individual pellets, which showed densities of ca. 90% of the theoretical one.

Results and discussion

X-ray diffraction and ^{19}F MAS NMR

In Fig. 3 the X-ray powder patterns of the starting materials as well as those of the mixtures, each milled for 10 h, are shown. For comparison, the patterns of nanocrystalline LaF_3 and SrF_2 are included as well. We clearly see that the reflections broaden when going from microcrystalline LaF_3 to the nanocrystalline sample. According to Scherrer's equation an average crystallite of ca. 18 nm is estimated for nano-LaF_3 prepared by ball milling. At first glance, substitution of La^{3+} ions by Sr^{2+} in the compositional range $0 < x \leq 0.1$ does not show a great effect on the lattice parameters of LaF_3, careful inspection of the patterns reveals slight shifts, which will be discussed below. Importantly, no other phases than LaF_3 were detected by X-ray diffraction. Thus, no decomposition products or other phases than $La_{1-x}Sr_xF_{3-x}$ have been formed. This observation is confirmed by high-resolution ^{19}F MAS NMR spectroscopy, which solely shows signals that can be attributed to F anions in $La_{1-x}Sr_xF_{3-x}$ (see below).

Careful inspection of the diffraction patterns shows that with increasing x the broadening of the reflections increases. Mixing two fluorides, which differ in Mohs hardness, might lead to smaller crystallites. In our case, however, Mohs' hardness of the fluorides is very similar (LaF_3 (4.5); SrF_2 (4)). Thus, the broadening is assumed to be also affected by lattice strain and disorder due to the mixed cation effect. Indeed lattice strain, when estimated using the method introduced by Williamson and Hall [30] increases from 0.0077 ($x = 0.01$) to 0.0107 ($x = 0.1$), see also Table 1. The estimated mean crystallite sizes $\langle d \rangle$ represent apparent values as they do not consider small distributions of lattice constants because of Sr^{2+} incorporation. As is exemplarily shown for the (2−11) reflection, see Fig. 3b, its position slightly shifts toward smaller diffraction angles 2θ. This shift is explained by lattice expansion due to successful heterovalent replacement of La^{3+} by the larger Sr^{2+} species. Refinement of the XRD patterns reveals that the lattice expands slightly along the c-axis (Table 1); note that all the values shown in Table 1 are to be regarded as rough estimates as we deal with broad reflections from nanocrystalline samples. A small distribution of lattice constants will contribute to the broadening effect. Thus, it is likely that the crystallite diameter of the samples does not change much with composition. ^{19}F MAS NMR, which locally probes the different magnetic environments seen by the F spins, also points to an increase in lattice distortions with increasing x, at least if we consider values larger than 0.01, see Table 1.

In Fig. 4 the ^{19}F MAS NMR spectra of microcrystalline and nanocrystalline LaF_3 are shown. The spectra have been deconvoluted with appropriate Voigt functions to analyze the areas under the three lines visible. The most intense one belongs to the F1 ions on the $12g$ position. The F ions F2 ($4d$) and F3 ($2a$) are attributed to the signals showing up at $\delta_{iso} = 28.9$ ppm and 20.9 ppm, respectively. NMR tells us that the (ideal) occupation ratio of 6:2:1 ($12g : 4d : 2a$) is almost fulfilled; experimentally we obtain 6:1.7:0.92 indicating vacant F sites in the La-rich regions of LaF_3. Because of charge neutrality one may suspect that we have a La deficient binary fluoride at hand where F anions preferentially fill the F1 sites rather than the F2 and F3 sites. Ball milling drastically
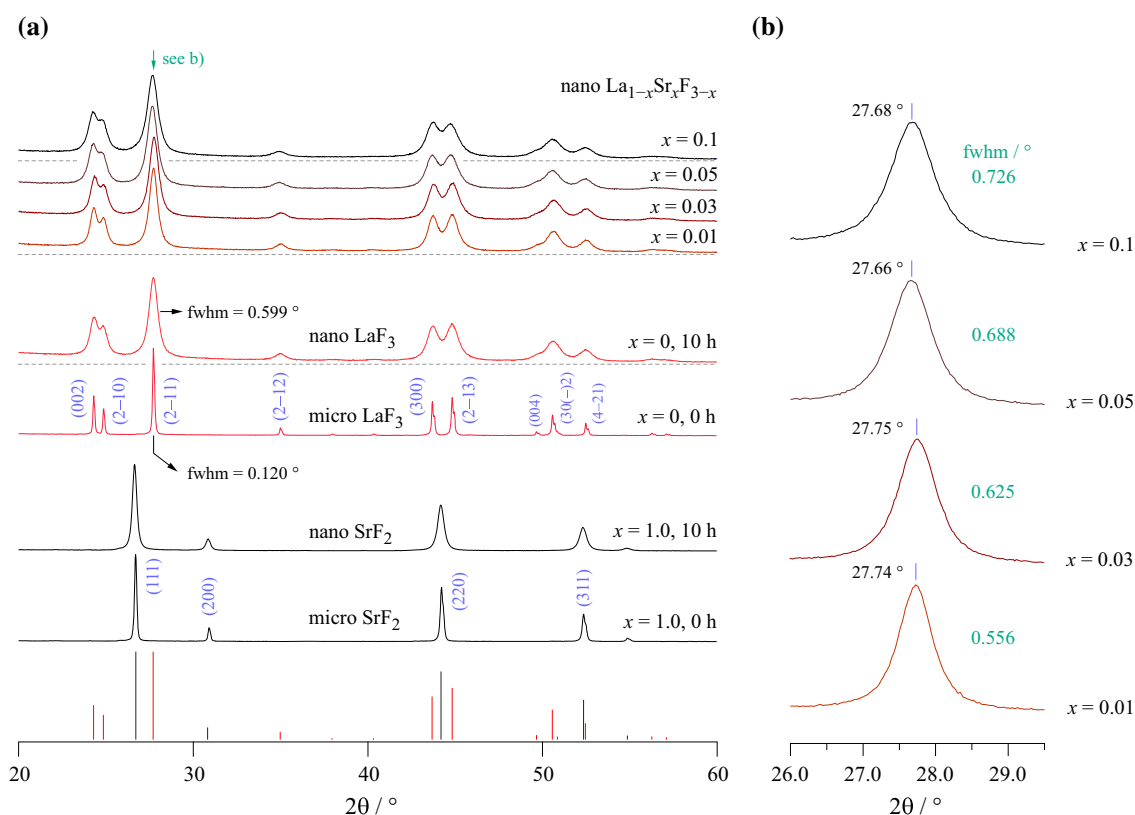
Figure 3 X-ray diffractograms of SrF_2 and LaF_3 as well as the mechanosynthesized cation-mixed ternary fluorides $La_{1-x}Sr_xF_{3-x}$. The nanocrystalline samples were obtained after 10 h of mechanical treatment in a planetary mill. Numbers in parentheses denote the hkl indices. The starting materials as well as the were phase pure; neither foreign phases nor abrasion from the vial sets used could be detected by X-ray diffraction. Broadening of the reflections is due to gain-size effects and strain introduced during milling. The reflection at $2\theta = 27.7°$ is shown in a magnified view in **b**. The slight shift toward lower diffraction angles shows the incorporation of larger Sr^{2+} ions into the tysonite structure of LaF_3. Broadening with increasing Sr content indicates increasing strain or distortions because of the cation mixing effect. An increasing extent of structural disorder upon mixing the two cations is also seen through ^{19}F MAS NMR, see below.

Table 1 Crystallite sizes ($\langle d \rangle$) and strain (ϵ) as estimated via Scherrer's equation and the method introduced by Williamson and Hall; values refer to mechanosynthesized, nanocrystalline $La_{1-x}Sr_xF_{3-x}$ obtained after a milling period of 10 h. Lattice parameters a and c are also included; for unmilled LaF_3 we obtained $a = 7.1886$ Å and $c = 7.3539$ Å

x	$\langle d \rangle$/nm	strain ϵ	a / Å	c / Å
0	18	0.0085	7.1882	7.3542
0.01	20	0.0077	7.1849	7.3533
0.03	17	0.0089	7.1876	7.3557
0.05	15	0.0101	7.1849	7.3536
0.10	14	0.0107	7.1833	7.3586

broadens the lines and reveals a large distribution of chemical shifts revolving around the original isotropic values. Importantly, it is no longer possible to reproduce the whole signal with only three lines. Instead, an additional broad line centered at $\delta_{iso} = -11$ ppm has to be considered to parameterize the overall NMR response. Most likely, this line represents F1 ions in distorted environments between the La-rich layers in lanthanum fluoride.

As an representative of the cation-mixed samples, the ^{19}F high-resolution MAS NMR spectrum of $La_{1-x}Sr_xF_{3-x}$ with $x = 0.1$ is presented in Fig. 5. Obviously, the mixed cation effect causes additional broadening of the NMR lines. Still, we are able to resolve the F1 and F2/F3 sites via MAS NMR. The line attributed to the F1 anions shifts toward lower ppm values as it has also been documented by Chable et al. in the literature before [24]. The signal at -85 ppm reveals a very tiny amount of residual SrF_2. Such small amount is difficult to be detected by X-ray
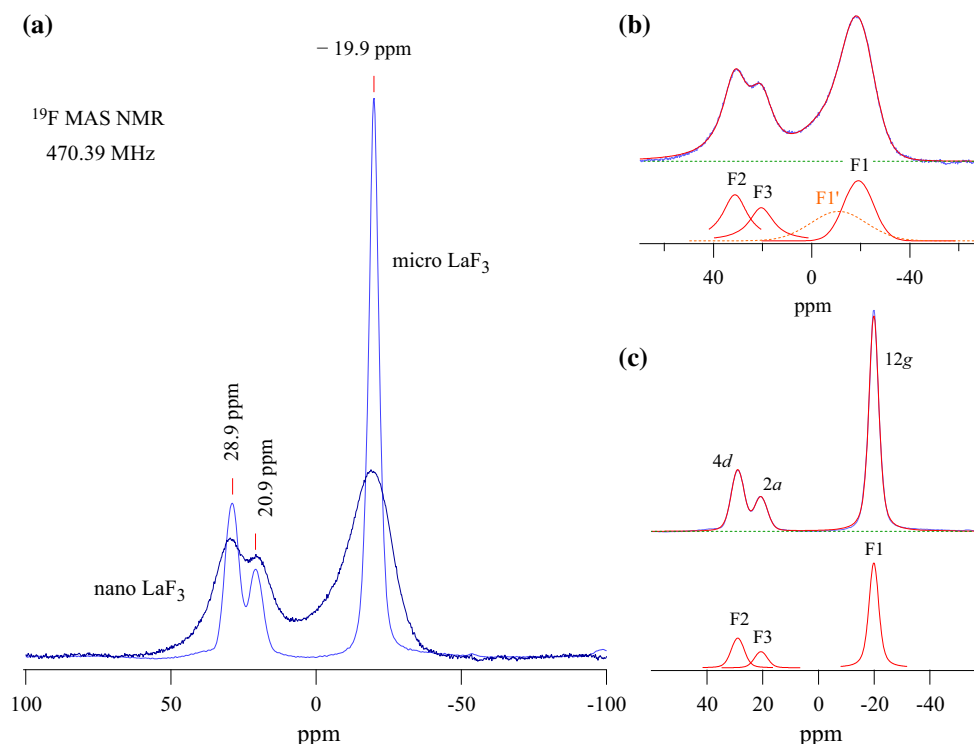
Figure 4 ^{19}F MAS NMR spectra recorded at 60 kHz rotation speed and 470.39 MHz: **a** spectra of microcrystalline and nanocrystalline LaF$_3$. The nanocrystalline sample was obtained after ball milling the microcrystalline material for 10 h in a planetary mill. **b** deconvolution of the spectra shown in **a** with appropriate Lorentzian functions. For nano LaF$_3$ the deconvolution is only possible after considering a fourth line centered at -11 ppm. Presumably, this line reflects F anion in the $_\infty[F_{2-x}]^{-2+x}$ interslab as its chemical shift is comparable to that of the original F1 ions. F jumps via vacancies along the F$_{12g}$–V$_{12g}$-F$'_{12g}$ pathway seems to be likely.

diffraction because of signal overlapping and its possible non-crystallinity.

In Fig. 5b we tried to reproduce the spectrum of nanocrystalline La$_{0.9}$Sr$_{0.1}$F$_{2.9}$ with appropriate Lorentzian-shaped functions that simply represent the F1 part and F2/F3 region of the spectrum, respectively. These lines have no further meaning as it is no longer possible to reproduce the original F sites with just one NMR line, either Gaussian, Lorentzian or a combination of both. The lines depicted are just used to highlight that the whole spectrum can only be parameterized if a broad line near 0 ppm is considered, see the dashed line in the lower graph of Fig. 5. As these additional NMR intensities needed to describe the spectrum are located near the center of the whole NMR response we suppose that besides the F1 sites also the F2 and F3 sites, to a minor extent, also contribute to overall F anion exchange, as has already assumed earlier for pure LaF$_3$ [20].

Worth noting, at ambient bearing gas temperature the MAS NMR lines can be well resolved. A single sharp single, which would be the result of a fast exchange processes leading to full coalescence of some or all of the signals, is not seen. Therefore, MAS NMR suggests, if we consider the spectral range the lines cover, F anion jump rates involving all of the available sites to be much lower than $10^5\,\text{s}^{-1}$. This estimation, which is valid for temperatures around ambient, is in good agreement with earlier NMR results [20] and the ionic conductivities probed here (see below). It points out the poor F anion mobility in LaF$_3$, even for nanostructured LaF$_3$ ionic conductivities are low compared to other ionic conductors, see Fig. 6 (and the next section) where the corresponding conductivity and permittivity isotherms of the sample with $x = 0.1$ are shown. According to Grey and co-workers the line representing the F1 anions starts to narrow at elevated temperatures before two distinct coalescence effects take place representing the F1–F3 exchange and F1–(F2,F3) exchange; for a microcrystalline sample with $x = 0.01$ full coalescence of all signals is only observed at $T \geq 266\,°C$.
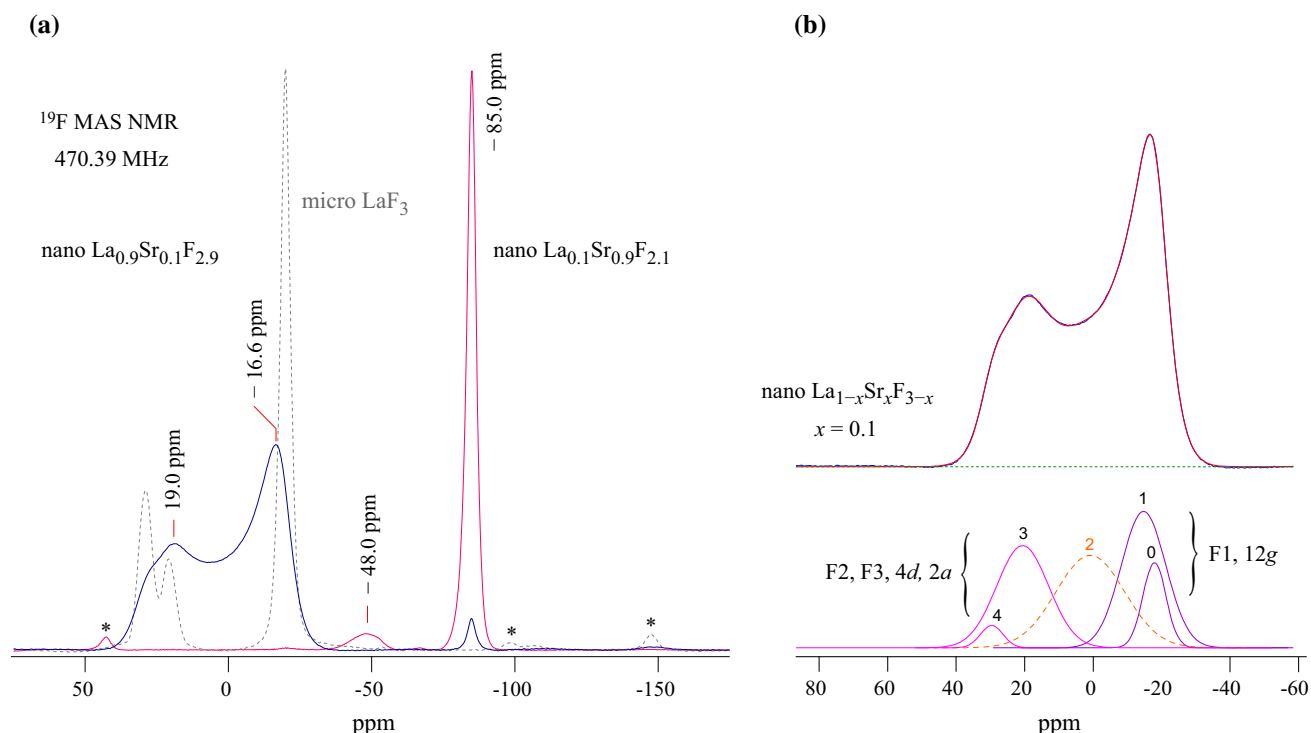
Figure 5 ^{19}F MAS NMR spectra of nanocrystalline $La_{1-x}Sr_xF_{3-x}$ with $x = 0.1$ as the nominal composition. In addition, the spectra of nano LaF_3 and $La_{1-x}Sr_xF_{3-x}$ with $x = 0.9$ are shown. Asterisks (∗) mark spinning side bands. In the Sr-rich sample crystallizing with $Fd\bar{3}m$ symmetry a new signal at -48 ppm is seen; most likely this line represents F anions near La centers. For $La_{0.9}Sr_{0.1}F_{2.9}$ broadened lines are seen slightly shifted to new positions as compared to those in microcrystalline Sr-free LaF_3. In **b** a formal deconvolution of the spectrum of $La_{0.9}Sr_{0.1}F_{2.9}$ is shown. As already seen for nano LaF_3, NMR intensities around 0 ppm show up which reveal F anions in mixed environments with distorted polyhedra, see the line drawn with a dashed line. See text for further explanations.

For comparison, in Fig. 5 the NMR spectrum of a Sr-rich compound, $La_{0.1}Sr_{0.9}F_{2.1}$ is shown that has been prepared in the same way as the other samples. $La_{0.1}Sr_{0.9}F_{2.1}$ crystallizes with SrF_2 structure. Apart from the prominent F NMR signal of SrF_2 a new line shows up at -48 ppm. It reflects the F anions near La ions in the mixed compound. The Sr-rich compounds are characterized by ionic conductivities that are lower than those of the La-rich fluorides. Therefore, here we focus on the samples that crystallize with the more complex tysonite structure. In the following section the change in ionic conductivity when going from pure LaF_3 to cation-mixed $La_{1-x}Sr_xF_{3-x}$ is presented.

Conductivity measurements

To probe ionic conductivities of both the microcrystalline and nanocrystalline samples, including the mixed ones, we recorded conductivity isotherms covering both a broad frequency range and a large temperature region. Exemplarily, in Fig. 6 the real part σ' of the complex conductivity (as well as the real part ϵ' of the complex permittivity) of mechanosynthesized $La_{0.9}Sr_{0.1}F_{2.9}$ is shown as a function of the frequency v covering a dynamic range of 9 orders of magnitude.

At high temperatures and low frequencies electrode polarization is seen as the F ions cannot pass the Au blocking electrodes used to measure the total electrical response. This response causes a significant, in many cases multistep, decrease of σ' in the low frequency limit. Here it is characterized by capacitances in the µF regime, values being typically expected for the piling up of ions near blocking electrodes. Most importantly, the conductivity isotherms reveal distinct frequency independent plateaus, denoted as P1 in Fig. 6b), from which we read off the so-called direct current values σ_{DC}. σ_{DC} refers to long-range ion transport through the macroscopic
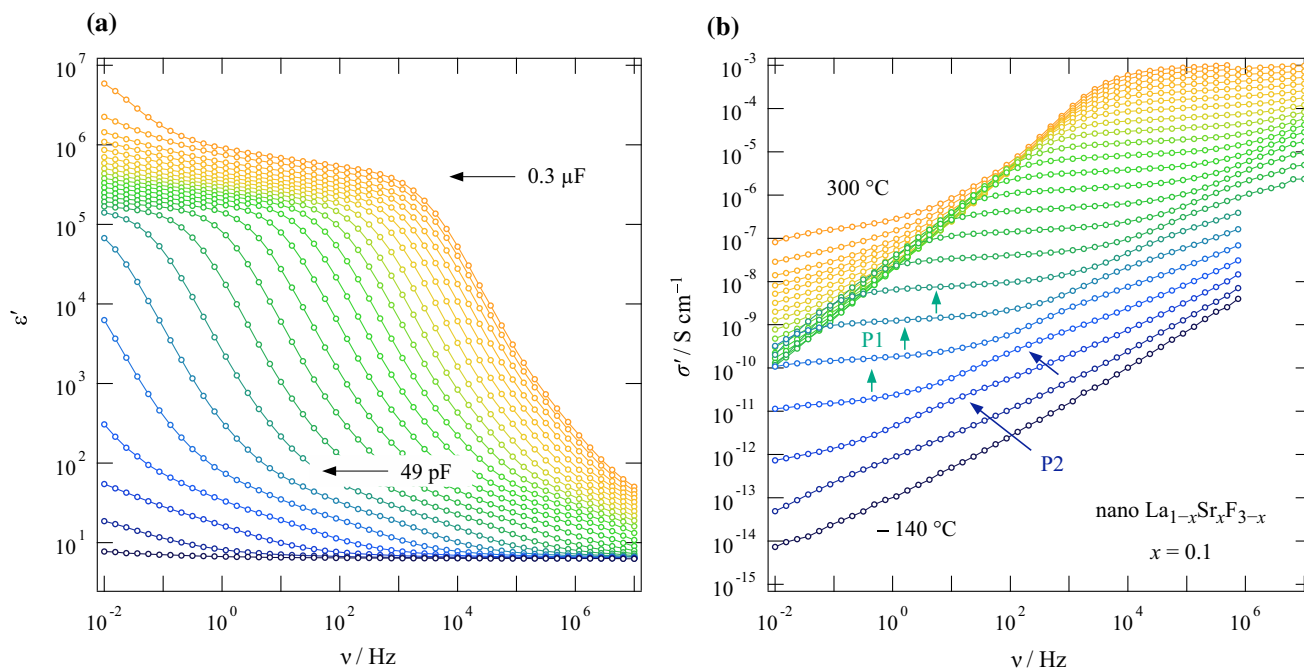
Figure 6 Permittivity spectra (**a**) and conductivity spectra (**b**) of nanocrystalline $La_{0.9}Sr_{0.1}F_{2.9}$. The isotherms were recorded at temperatures ranging from $-140\,°C$ to $300\,°C$ in steps of 20 °C. Besides electrode polarization, which is seen at the best at high temperatures (see also **a**), the conductivity spectra measured at low T (see **b**) reveal two distinct electrical responses marked as P1 and P2.

sample. Here, at ambient temperature the capacitance C associated with this main electrical process turned out to be in the order of 38 pF. This value was derived from analyzing the corresponding complex plane plots, that is, Nyquist diagrams, which were obtained by plotting the imaginary part of the complex impedance as a function of its real part. Capacitances of a few pF usually suggest σ_{DC} to be related to a bulk response. The relatively high value of ca. 38 pF indicates that the response causing P1 is partly affected by the surface-influenced areas of the nm-sized crystallites. A second plateau (P2), only poorly visible at higher T but recognizable in the isotherms measured at the lowest temperatures, also points to a bulk response. We attribute this shallow plateau to ion dynamics in the inner core of the nanocrystals (see the arrows in Fig. 6b).

From the corresponding Nyquist diagrams the faster relaxation processes, corresponding to P2, cannot be resolved properly. Instead, it is well seen if we plot the imaginary part M'' of the complex modulus vs. frequency, see Fig. 7a. At sufficiently low temperature two relaxation peaks, M1 and M2, are visible (see red arrows), which are separated by almost two orders of magnitude on the frequency

scale. This separation agrees well with the ratio $\sigma_{DC,P2}/\sigma_{DC,P1}$. While the peak with the larger amplitude corresponds to P2 in $\sigma'(\nu)$, the weaker one represents an electrical process with a longer (characteristic) relaxation time (P1). As M'' is proportional to the inverse of the capacitance, $M'' \propto 1/C$, peak M2 is characterized by an even lower capacitance C (ca. 25 pF) than that estimated for response P1. This lower capacitance underpins our assumption that plateau P2 reflects ion dynamics in the crystalline bulk regions.

In Fig. 7b the DC conductivities, plotted as $\sigma_{DC}T$, of the plateaus P1 and P2 are shown as a function of the inverse temperature. While the values corresponding to P1 follow Arrhenius behavior, $\sigma_{DC}T = \sigma_0 \exp(-E_a/(k_BT))$, with an activation energy of 0.49(1) eV, those of P2 slightly deviate from the Arrhenius line governing ion dynamics above 220 K. At higher temperatures we found an activation energy E_a of 0.45(3) eV, which is slightly lower than that determining P1.

An overview of the change in ionic conductivity in nanocrystalline $La_{1-x}Sr_xF_{3-x}$ is finally given in Fig. 8. Table 2 compares the activation energies obtained with the pre-factors σ_0. Microcrystalline SrF_2 shows
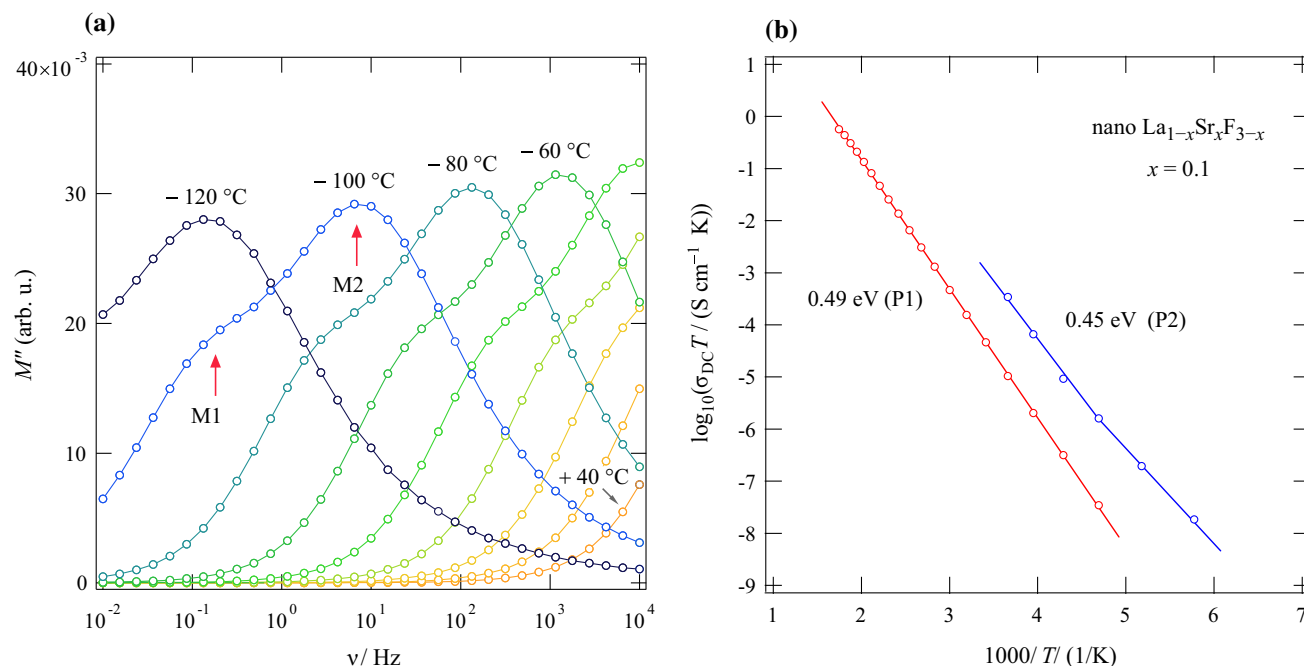
Figure 7 **a** Modulus representation of the data. As suggested by the conductivity isotherms two distinct peaks are visible denoted as M1 and M2. **b** Arrhenius representation of $\sigma_{DC}T(1/T)$; σ_{DC} was read off from the plateaus P1 and P2 (see Fig. 6b). The solid lines show fits with an Arrhenius law yielding activation energies for the P1 response slightly lower than 0.5 eV.

the lowest conductivities with an activation energy as high as 1.13 eV. Ball milling for 10 h leads to an increase of σ_{DC} by approximately one order of magnitude; accordingly, E_a slightly decreases to 1.04 eV. A very similar situation is found for LaF_3 although the original conductivity of coarse-grained lanthanum fluoride, if we consider values at $T = 440$ K, exceeds that of SrF_2 by 4 orders of magnitude. Through heterovalent replacement of the La cations the overall conductivity can be further increased reaching values that compete with those found for mechanosynthesized $La_{1-x}Ba_xF_{3-x}$ [10, 37], which takes advantage of an even larger size mismatch of the mixed cations [38]. Obviously, the mismatch in size in the Sr-compound is already large enough to reach the upper limit of σ_{DC}, at least if mechanosynthesized samples are considered. The activation energy of tysonite-type $La_{0.9}Ba_{0.1}F_{2.9}$, which has been studied in detail in [10, 37], is comparable to that of the Sr analogue. Just for comparison, ion transport in $La_{0.9}Ba_{0.1}F_{2.9}$ [31] turned out to be clearly higher than that in metastable and nanocrystalline $Ba_{0.5}Ca_{0.5}F_2$ [32], which crystallizes with cubic symmetry and which has been studied earlier by some of us [15, 32].

For the sake of clarity, for most of the samples only the values referring to P1 have been included in

Fig. 7. For the sample with $x = 0.1$ we also inserted the conductivities corresponding to plateau P2. The latter values, if extrapolated to higher T, exceed those of a $LaF_3|SrF_2$ multilayer system, which has been prepared by molecular beam epitaxy (MBE) and discussed in literature quite recently [33]. The spacing of the heterolayer sample was 25 nm. In such a sample, besides any possible mixing effect directly at the interfaces, ion movements in space-charge zones [6, 39–42] are anticipated to govern ionic conductivity. Worth mentioning, the conductivity of the $LaF_3|SrF_2$ hetero-layers shown reflects the longitudinal one, i.e., the values represent ion transport perpendicular to the fluoride layers. In this ionic conductor overlapping space-charge zones are assumed to enable fast ion transport even perpendicular to the hetero-interfaces. The most prominent example for this kind of artificial ion conductor is epitaxially grown $BaF_2|CaF_2$ [6].

For comparison, a mixed $La_{1-x}Sr_xF_{3-x}$ sample, which has also been prepared by MBE [33], is shown in Fig. 8, too. Interestingly, the conductivities from plateau P2 of our mechanosynthesized nanocrystalline sample with $x = 0.1$ are at least comparable with these results. This finding indicates that $La_{1-x}Sr_xF_{3-x}$ powders with transport properties
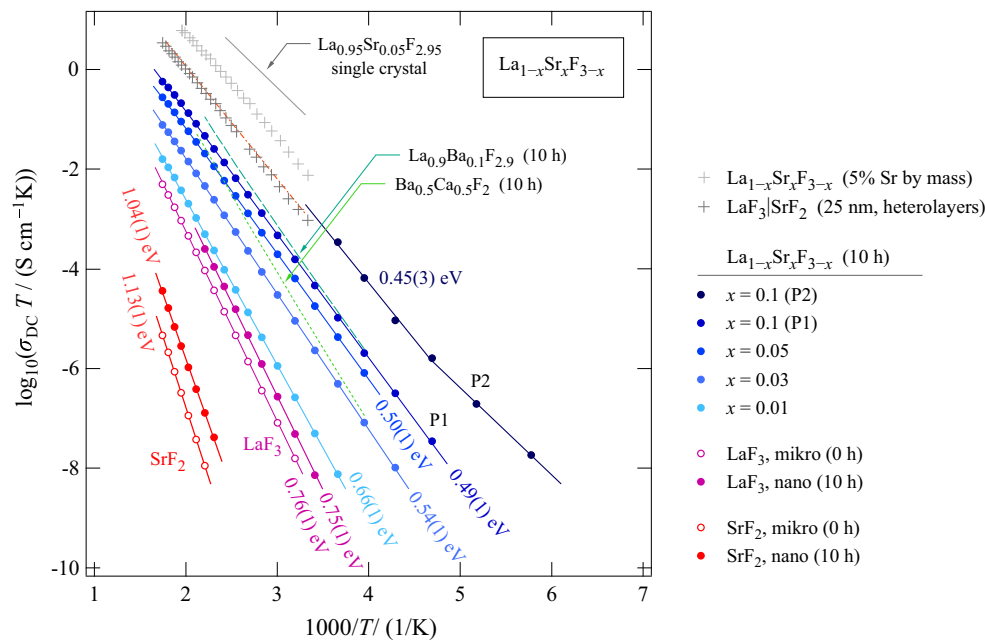
Figure 8 Arrhenius plot of the ion conductivities ($\sigma_{DC}T$ vs. $1000/T$) of cation-mixed nanocrystalline $La_{1-x}Sr_xF_{3-x}$. Solid lines represent fits with Arrhenius equations yielding the activation energies E_a indicated. For comparison, the coarse-grained starting materials as well as LaF_3 and SrF_2 milled for 10 h are also shown. The dashed lines represent values of $\sigma_{DC}T$ of two further ternary fluorides already presented and discussed in literature viz. $La_{1-x}Ba_xF_{3-x}(x = 0.1)$ [31] and $Ba_{1-x}Ca_xF_2(x = 0.5)$ [32]; here, we have prepared these two reference materials by milling the respective starting materials for 10 h. Crosses indicate conductivities taken from literature [33]: the data points show conductivities of

$La_{1-x}Sr_xF_{3-x}$ with 5 mass-% Sr and ion transport properties of multilayer $LaF_3|SrF_2$ heterostructures with an interfacial spacing of 25 nm. These samples were prepared by molecular beam epitaxy, see [33]. For the sake of completeness, also results from a $La_{0.95}Sr_{0.05}F_{2.95}$ single crystal and mechanosynthesized, but annealed, $La_{0.95}Sr_{0.05}F_{2.95}$ (dashed-dotted line, the values almost coincide with the $LaF_3|SrF_2$ multilayer system) are included [34, 35]. Space-charge and segregation effects might be used to explain the decrease in ionic conductivity when going from single crystals to nm-sized systems with high surface areas [36].

Table 2 Comparison of activation energies E_a and pre-factors σ_0 of the Arrhenius lines shown in Fig. 8. The values refer to the mechanosynthesized, nanocrystalline samples $La_{1-x}Sr_xF_{3-x}$. The uncertainty of E_a is in the last digit, for σ_0 it is roughly $\pm 0.1\,S\,cm^{-1}K$

x	E_a/eV	$\log_{10}(\sigma_0/(S\,cm^{-1}K))$	Remarks
0	0.75	4.79	
0.01	0.66	4.04	
0.03	0.54	3.65	
0.05	0.50	3.87	
0.10	0.49	4.13	P1
0.10	0.45	4.81	P2
0.05	0.45	4.55	Milled, annealed [34, 35]
0.05	0.35	4.95	Single crystal [34]

being similar to those of MBE grown films can be made available also by high-energy ball milling. Of course, ball milling is a much more feasible technique able to produce large quantities of powders [25].

If we consider $La_{1-x}Sr_xF_{3-x}$ samples prepared differently and with different morphologies and preparation histories than here, see, e.g., the systematic studies by Sorokin and Sobolev [34], we find that $\sigma_{DC}T$ of P2 is considerably lower than that what is usually found for a $La_{0.95}Sr_{0.05}F_{2.95}$ single crystal. σ of a mechanosynthesized, but annealed sample is slightly lower than $\sigma_{DC}T$ of P2, see Fig. 8 and Table 2, which also includes the corresponding activation energies and pre-factors (see below). To our knowledge and understanding, the origin of this decrease is not fully understood yet. At first glance, one might speculate that grain-boundary regions might block long-range ion transport. Here, we could not find strong evidence that the conductivities measured reflect ion transport across grain boundaries. They mainly refer, as far as electrical capacitances are considered, to bulk properties. This assignment is in agreement with ^{19}F NMR line shape measurements. Conductivities in the mS range at room temperature

would translate into very fast F exchange processes as reported for single crystals. Even if such processes were hidden in our samples as non-ascertainable electric bulk property, they should produce strongly motionally narrowed NMR lines. Such lines are absent in our case. The bulk ion dynamics in mechanosynthesized $La_{1-x}Sr_xF_{3-x}$ does not reach the conductivities reported for the single crystalline state. The situation resembles that of Durá et al. [36] who studied oxygen ion conductivity in nanostructured ZrO_2. The authors presented indications of an extended space-charge layer because of oxygen vacancy segregation in the grain-boundary core region. This effect leads to charge carrier depletion in the grain leading to a decrease in oxygen ion conductivity. Such segregation and space-charge effects might be useful to also explain the discrepancy seen between nm-sized polycrystalline fluorides on the one hand and single crystals on the other.

Going back to the samples studied here, the increase in σ_{DC} for mechanosynthesized $La_{1-x}Sr_xF_{3-x}$ powder samples (Fig. 8, Table 2) seems to be mainly driven by the decrease in migration barrier. Indeed, E_a sharply decreases from 0.75 eV ($x = 0$) to 0.54 eV ($x = 0.03$) if only a tiny amount of Sr^{2+} ions were incorporated into the tysonite structure, see also Table 2. The lowering of the activation energy is, however, accompanied by a decrease of the Arrhenius pre-factor σ_0, which partly compensates for the enhancement in ionic conductivity. In particular, a low σ_0 has an impact on conductivities at high temperatures rather than at lower T.

The trend shown in Table 2 is in fair agreement with this so-called Meyer-Neldel rule [43], an enthalpy-entropy compensation effect. This compensation effect is based on a linear dependence of the pre-factor on the activation enthalpy (or energy). The higher the activation enthalpy, the higher the pre-factor σ_0, which is affected by entropy contributions, attempt frequencies and, in the case of ionic conductivity, also by the effective number of charge carriers. Careful inspection of σ_0 reveals that, for values of x larger than 0.03, the pre-factor increases again. This increase tells us that, while E_a remains almost constant for compositions above $x = 0.03$, the further enhancement of σ_{DC} is driven by σ_0 rather than by E_a. A similar observation has been quite recently reported for mechanosynthesized samples of $Ba_{1-x}Ca_xF_2$ [32].

In the low-concentration limit ($x \leq 0.1$), which we focused on here, we do not expect large changes in attempt frequencies. Instead, in this compositional regime contributions of both the migration and configurational entropy as well as the effective number of charge carriers are expected to govern σ_0. After E_a has reached its limiting value of ca. 0.5 eV these effects take over and allow the ions to move quickly in a disordered potential landscape generated by size mismatch.

Conclusions

Mechanosynthesis is a versatile tool to prepare cation-mixed fluorides that exhibit ion transport properties greatly exceeding those of their nanocrystalline but binary fluorides. By taking advantage of high-energy planetary mills we showed how poorly conducting LaF_3 can be turned into a highly conducting material via heterovalent replacement strategies. Already at low substitution levels of $x = 0.1$ the ionic conductivity of $La_{1-x}Sr_xF_{3-x}$ can be significantly improved when referenced to that of pure, nanocrystalline LaF_3. After 10 h of mechanical treatment under dry conditions, a phase pure powder is obtained that is characterized by high F anion conductivities ($1 \times 10^{-5}\,S\,cm^{-1}$ (373 K)) and relatively low activation energies of 0.49 eV. Structural disorder and lattice strain, being a result of mixing cations differing in ionic radii, is assumed to cause the increase in ionic conductivity observed. ^{19}F MAS NMR clearly supports this idea as the lines reveal a broadened lines pointing to a distribution of chemical shifts. This distribution is caused by point defects, particularly vacant F sites, and polyhedra distortions in the mechanically treated samples. These features facilitate rapid anion exchange that boosts ionic conductivity. For $x > 0.03$ the Arrhenius pre-factor rather than the activation energy is responsible for the increase in σ_{DC} with increasing Sr content.

Acknowledgements

in the frame of the priority program *crystalline non-equilibrium phases* (SPP 1415). Further support by the FFG K-project *safe battery* is highly appreciated.

Open Access This article is distributed under the terms of the Creative Commons Attribution 4.0 International License (http://creativecommons.org/licenses/by/4.0/), which permits unrestricted use, distribution, and reproduction in any medium, provided you give appropriate credit to the original author(s) and the source, provide a link to the Creative Commons license, and indicate if changes were made.

References

[1] Knauth P (2009) Inorganic solid Li ion conductors: an overview. Solid State Ion 180(14–16):911

[2] Tuller HL (2000) Ionic conduction in nanocrystalline materials. Solid State Ion 131(1):143

[3] Fergus JW (1997) The application of solid fluoride electrolytes in chemical sensors. Sens Act B: Chem 42(2):119–130

[4] Whittingham MS (2004) Lithium batteries and cathode materials. Chem Rev 104:4271

[5] Bachman JC, Muy S, Grimaud A, Chang H-H, Pour N, Lux SF, Paschos O, Maglia F, Lupart S, Lamp P, Giordano L, Shao-Horn Y (2016) Inorganic solid-state electrolytes for lithium batteries: mechanisms and properties governing ion conduction. Chem Rev 116(1):140–162

[6] Sata N, Eberman K, Eberl K, Maier J (2000) Mesoscopic fast ion conduction in nanometre-scale planar heterostructures. Nature 408:946

[7] Reddy MA, Fichtner M (2011) Batteries based on fluoride shuttle. J Mater Chem 21:17059–17062

[8] Rongeat C, Reddy MA, Witter R, Fichtner M (2013) Nanostructured fluorite-type fluorides as electrolytes for fluoride ion batteries. J Phys Chem C 117(10):4943

[9] Rongeat C, Anji Reddy M, Witter R, Fichtner M (2014) Solid electrolytes for fluoride ion batteries: ionic conductivity in polycrystalline tysonite-type fluorides. ACS Appl Mater Interf 6(3):2103–2110

[10] Preishuber-Pflügl F, Bottke P, Pregartner V, Bitschnau B, Wilkening M (2014) Correlated fluorine diffusion and ionic conduction in the nanocrystalline F$^-$ solid electrolyte Ba$_{0.6}$La$_{0.4}$F$_{2.4}$ - ^{19}FT$_{1(\rho)}$ NMR relaxation vs. conductivity measurements. Phys Chem Chem Phys 16:9580

[11] Sorokin NI, Sobolev BP (2007) Nonstoichiometric fluorides—solid electrolytes for electrochemical devices: a review. Cryst Rep 52(5):842–863

[12] Preishuber-Pflügl F, Wilkening M (2016) Mechanochemically synthesized fluorides: local structures and ion transport. Dalton Trans 45:8675

[13] Ruprecht B, Wilkening M, Steuernagel S, Heitjans P (2008) Anion diffusivity in highly conductive nanocrystalline BaF$_2$: CaF$_2$ composites prepared by high-energy ball milling. J Mater Chem 18:5412

[14] Ruprecht B, Wilkening M, Feldhoff A, Steuernagel S, Heitjans P (2009) High anion conductivity in a ternary non-equilibrium phase of BaF$_2$ and CaF$_2$ with mixed cations. Phys Chem Chem Phys 11:3071

[15] Düvel A, Ruprecht B, Heitjans P, Wilkening M (2011) Mixed alkaline-earth effect in the metastable anion conductor Ba$_{1-x}$Ca$_x$F$_2$ ($0 \leq x \leq 1$): correlating long-range ion transport with local structures revealed by ultrafast ^{19}F MAS NMR. J Phys Chem C 115(48):23784

[16] Heitjans P, Masoud M, Feldhoff A, Wilkening M (2007) NMR and impedance studies of nanocrystalline and amorphous ion conductors: lithium niobate as a model system. Faraday Discuss 134:67

[17] Wilkening M, Epp V, Feldhoff A, Heitjans P (2008) Tuning the Li diffusivity of poor ionic conductors by mechanical treatment: high Li conductivity of strongly defective LiTaO$_3$ nanoparticles. J Phys Chem C 112(25):9291

[18] Wohlmuth D, Epp V, Bottke P, Hanzu I, Bitschnau B, Letofsky-Papst I, Kriechbaum M, Amenitsch H, Hofer F, Wilkening M (2014) Order vs. disorder—a huge increase in ionic conductivity of nanocrystalline LiAlO$_2$ embedded in an amorphous-like matrix of lithium aluminate. J Mater Chem A 2:20295–20306

[19] Prutsch D, Breuer S, Uitz M, Bottke P, Langer J, Lunghammer S, Philipp M, Posch P, Pregartner V, Stanje B, Dunst A, Wohlmuth D, Brandstätter H, Schmidt W, Epp V, Chadwick A, Hanzu I, Wilkening M (2017) Nanostructured ceramics: ionic transport and electrochemical activity. Z Phys Chem 231:1361

[20] Wang F, Grey CP (1997) Probing the mechanism of fluoride-ion conduction in LaF$_3$ and strontium-doped LaF$_3$ with high-resolution ^{19}F MAS NMR. Chem Mater 9(5):1068–1070

[21] Šepelák V, Düvel A, Wilkening M, Becker K-D, Heitjans P (2013) Mechanochemical reactions and syntheses of oxides. Chem Soc Rev 42:7507

[22] Düvel A, Wegner S, Efimov K, Feldhoff A, Heitjans P, Wilkening M (2011) Access to metastable complex ion conductors viamechanosynthesis: preparation, microstructure and conductivity of (Ba,Sr)LiF$_3$ with inverse perovskite structure. J Mater Chem 21:6238

[23] Breuer S, Stanje B, Pregartner V, Lunghammer S, Hanzu I, Wilkening M (2018) Fluorine translational anion dynamics

in nanocrystalline ceramics: SrF_2-YF_3 solid solutions. Crystals 8(3):122

[24] Chable J, Dieudonne B, Body M, Legein C, Crosnier-Lopez M-P, Galven C, Mauvy F, Durand E, Fourcade S, Sheptyakov D, Leblanc M, Maisonneuve V, Demourgues A (2015) Fluoride solid electrolytes: investigation of the tysonite-type solid solutions $La_{1-x}Ba_xF_{3-x}(x < 0.15)$. Dalton Trans 44:19625–19635

[25] Chable J, Martin A, Bourdin A, Body M, Legein C, Jouanneaux A, Crosnier-Lopez M-P, Galven C, Dieudonne B, Leblanc M, Demourgues A, Maisonneuve V (2017) Fluoride solid electrolytes: from microcrystalline to nanostructured tysonite-type $La_{0.95}Ba_{0.05}F_{2.95}$. J Alloys Comp 692:980–988

[26] Dieudonné B, Chable J, Mauvy F, Fourcade S, Durand E, Lebraud E, Leblanc M, Legein C, Body M, Maisonneuve V, Demourgues A (2015) Exploring the $Sm_{1-x}Ca_xF_{3+x}$ tysonite solid solution as a solid-state electrolyte: relationships between structural features and F^- ionic conductivity. J Phys Chem C 119(45):25170–25179

[27] Scherrer P (1918) Bestimmung der Größe und der inneren Struktur von Kolloidteilchen mittels Röntgenstrahlen. Nachr Ges Wiss Göttingen 2:98

[28] Patterson AL (1939) The scherrer formula for x-ray particle size determination. Phys Rev 56:978–982

[29] Sadoc A, Body M, Legein C, Biswal M, Fayon F, Rocquefelte X, Boucher F (2011) NMR parameters in alkali, alkaline earth and rare earth fluorides from first principle calculations. Phys Chem Chem Phys 13:18539–18550

[30] Williamson G, Hall W (1953) X-ray line broadening from filed aluminium and wolfram. Acta Metall 1(1):22

[31] Breuer S, Wilkening M (To be published; manuscript under preparation)

[32] Breuer S, Wilkening M (2018) Mismatch in cation size causes rapid anion dynamics in solid electrolytes: the role of the arrhenius pre-factor. Dalton Trans 47:4105–4117

[33] Vergentev T, Banshchikov A, Filimonov A, Koroleva E, Sokolov N, Wurz MC (2016) Longitudinal conductivity of LaF_3/SrF_2 multilayer heterostructures. Sci Tech Adv Mater 17(1):799–806

[34] Sorokin NI, Sobolev BP (2016) Fluorine-ion conductivity of different technological forms of solid electrolytes $R_{1-y}M_yF_{3-y}$ (LaF_3 type) (M = Ca, Sr, Ba; R are rare earth elements). Cryst Rep 61(3):499–505

[35] Sorokin NI, Ivanovskaya NA, Sobolev BP (2014) Ionic conductivity of cold-pressed ceramics from grinding of $R_{0.95}M_{0.05}F_{2.95}$ solid electrolytes (R = La, Nd; M = Ca, Sr, Ba) synthesized by reaction in melt. Cryst Rep 59(2):248–251

[36] Durá OJ, López de la Torre MA, Vázquez L, Chaboy J, Boada R, Rivera-Calzada A, Santamaria J, Leon C (2010) Ionic conductivity of nanocrystalline yttria-stabilized zirconia: grain boundary and size effects. Phys Rev B 81:184301

[37] Düvel A, Bednarcik J, Šepelák V, Heitjans P (2014) Mechanosynthesis of the fast fluoride ion conductor $Ba_{1-x}La_xF_{2+x}$: from the fluorite to the tysonite structure. J Phys Chem C 118(13):7117–7129

[38] Cazorla C, Sagotra AK, King M, Errandonea D (2018) High-pressure phase diagram and superionicity of alkaline earth metal difluorides. J Phys Chem C 122(2):1267–1279

[39] Maier J (2005) Nanoionics: ion transport and electrochemical storage in confined systems. Nature Mater 4(11):805

[40] Maier J (2003) Nano-ionics: trivial and non-trivial size effects on ion conduction in solids. Z Phys Chem Int Ed 217(4):415

[41] Maier J (1995) Ionic conduction in space charge regions. Prog Solid State Chem 23(3):171

[42] Puin W, Rodewald S, Ramlau R, Heitjans P, Maier J (2000) Local and overall ionic conductivity in nanocrystalline CaF_2. Solid State Ion 131(1):159

[43] Meyer W, Neldel H (1937) Concerning the relationship between the energy constant epsilon and the quantum constant alpha in the conduction-temperature formula in oxydising semi-conductors. Phys Z 38:1014–1019